ELSEVIER

Combined forced and natural convection heat transfer in a deep lid-driven cavity flow

Ajay K. Prasad
Department of Mechanical Engineering, University of Delaware, Newark, DE

Jeffrey R. Koseff
Environmental Fluid Mechanics Laboratory, Stanford University, Stanford, CA

In this study, we describe the combined forced and natural convection (also known as mixed-convection) heat transfer process within a recirculating flow in an insulated lid-driven cavity of rectangular cross section (150 mm × 450 mm) and depth varying between 150 mm and 600 mm. The forced convection is induced by a moving lid, which shears the surface layer of the fluid in the cavity, thereby setting up a recirculating flow, while the natural convection flow is induced by heating the lower boundary and cooling the upper one. By appropriately varying the lid speed, the vertical temperature differential, and the depth, we obtained Gr/Re^2 ratios for these flows from 0.1 to 1000. Flow visualization using liquid crystals and heat flux measurements at specific locations over the lower boundary provided an insight into the nature of the heat transfer process under different flow and temperature conditions. The mean heat flux values over the entire lower boundary were analyzed to produce Nusselt number and Stanton number correlations which should be useful for design applications.

Keywords: Lid-driven cavity flow; forced and natural convection; thermochromic liquid crystals

Introduction

Heat transfer in flows in which the influence of forced convection and natural convection are of comparable magnitude (commonly referred to as "mixed-convection" flows) occur frequently in engineering situations. Gebhart (1971) separates mixed-convection processes into external flows and internal flows and provides a review of some of the more common geometries. Mixed-convection flows may be further subdivided into those where the inertia force is parallel to the buoyancy force and those where the inertia force is perpendicular to the buoyancy force. Lloyd and Sparrow (1970) developed a similarity solution for a mixed-convection flow on a vertical surface for a range of Prandtl numbers; in this study, the forced-convection flow aided the free-convection component. Siebers (1983) carried out experiments with a heated vertical wall in the presence of a cross stream, with a view towards predicting the behavior of a central receiving station in a solar power plant. Kays and Crawford (1993) list a number of studies of mixed convection over horizontal plates. For example, Wang et al. (1983) conducted heat transfer measurements in a water channel flow that was uniformly heated from below and compared their results with existing correlations. Similarly, Imura et al. (1978) focused on the transition from the laminar to the turbulent regime, by measuring the heat flux on a horizontal heated plate. At about the same time, a numerical investigation of a mixed convection boundary-layer flow on a horizontal surface was performed by Chen et al. (1977).

All the studies mentioned in the preceding paragraph pertain to external flows. However, internal, or confined, flows are also of great interest to designers of such alternate energy systems as solar ponds and solar storage devices. For example, Muñoz and Zangrando (1986) describe an experimental investigation of mixing in a double-diffusive fluid layer. They studied the effect of surface shear as well as bottom heating on entrainment and developed correlations for the same. Cha and Jaluria (1984) performed a numerical investigation of a recirculating mixed-convection flow in a stratified energy storage system, involving withdrawal of hot fluid and discharge of cold fluid into the storage chamber. For the range of governing parameters studied, their results indicate that the recirculating flow is strongly affected by buoyancy, as well as the geometry. In addition, the cooling of electronic components on a printed circuit board, and the heat transfer from rectangular cut-outs on the surface of a heat exchanger in the presence of an oncoming stream could also

Address reprint requests to Prof. A. K. Prasad, Department of Mechanical Engineering, University of Delaware, Newark, DE 19716, USA.

Received 7 January 1996; accepted 16 April 1996

Int. J. Heat and Fluid Flow 17: 460–467, 1996

655 Avenue of the Americas, New York, NY 10010

0142-727X/96/$15.00
PII S0142-727X(96)00054-6

be modeled as internal or recirculating flows, and provide a special incentive for our study.

The configuration described in the present investigation consists of an internal flow within a rectangular cavity driven by two mechanisms. First, by shearing the surface layer by means of a lid moving at a constant velocity, we induce a forced-convection flow within the cavity (see Figure 1). The lid speed can be increased continuously to produce Reynolds numbers, (Re, based on the lid speed U_B and the cavity width B) up to 12,000. This recirculating motion is extremely complex and three-dimensional (3-D) in nature and has been described in detail by Koseff and Street (1984) and Prasad et al. (1988). Second, by heating the lower boundary of the cavity and cooling the upper boundary, we can create a natural convection flow, as described by Rhee et al. (1985). The temperature differential between the lower and upper boundaries and the depth of the cavity D can be varied to obtain Grashof numbers for these flows (Gr, based on the cavity depth) between 10^7 and 5×10^9. The simultaneous use of both forcing mechanisms enables us to create flows in which the parameter Gr/Re^2 varies between 0.1 and 1000. By varying the dimensions of the cavity, it is also possible to create flows of widely differing geometric attributes, yet possessing the same Gr/Re^2 ratio.

Flow visualization using thermochromic liquid crystals (TLC) provides a simultaneous view of the temperature and velocity fields, thereby identifying the relevant flow structures and their influence on the heat transfer mechanisms in the cavity. This was supplemented by quantitative data, in the form of heat flux measurements at specific locations over the lower boundary, using microfoil heat flux sensors. The heat flux data in this paper are averaged over the entire lower boundary of the cavity (hereafter referred to as the cavity floor).

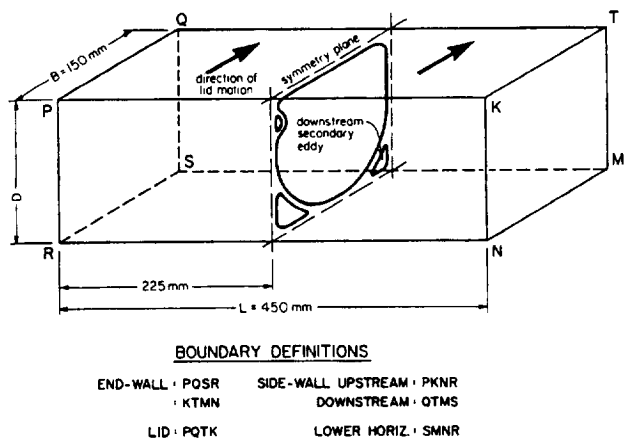

Figure 1 Definitions for the lid-driven cavity flow

The ratio Gr/Re^2 traditionally has been used to represent the relative magnitudes of forced and natural convection in a mixed-convection flow. In our configuration, we have produced the same value of the ratio, but by using different combinations of ΔT, D, and U_B. By examining the heat flux from these different cases, we want to determine if the ratio Gr/Re^2 is sufficient to characterize this class of mixed-convection flows, or if it needs to be modified by such factors as the depthwise aspect ratio (DAR).

Facility and instrumentation

The lid-driven cavity facility

The lid-driven cavity facility, constructed from 12.5-mm thick Plexiglas, consists of two attached "shoe-boxes," as shown in Figure 2. The lower of the two boxes is the main area of interest. It is rectangular in cross section, with streamwise width (B) of 150 mm, spanwise length (L) of 450 mm, and depth (D) varying between 150 and 600 mm. The upper box houses the lid and its driving system, which consists of a variable speed motor connected by a chain drive to one of a pair of rollers. The "lid" is a 0.08-mm thick copper belt, which is mounted on and driven by the two rollers. During operation, the belt-and-drive assembly in Figure 2 is lowered down into the upper box so that the belt just

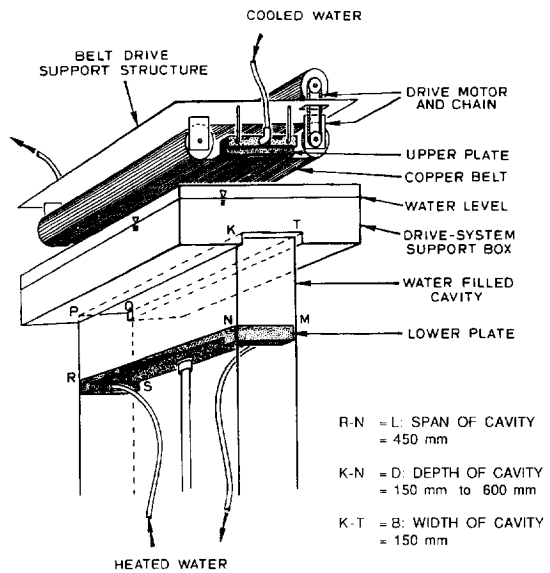

Figure 2 The lid-driven cavity facility (from Koseff and Street 1984)

Notation

B	cavity width
c_p	specific heat of water
D	cavity depth
g	acceleration due to gravity
Gr	Grashof number based on cavity depth
h	heat transfer coefficient
k	thermal conductivity of water
L	cavity length or span
Nu	Nusselt number based on cavity depth
q	heat flux (W/m^2)
Re	Reynolds number based on lid velocity and cavity width
St	Stanton number based on lid velocity
U_B	lid velocity

Greek

α	thermal diffusivity of water
β	thermal expansion coefficient of water
ΔT	temperature difference between lower (hotter) and upper (colder) cavity boundaries
ν	kinematic viscosity of water
ρ	density of water

touches the upper edges of the working area. The belt speed can be varied continuously to produce Reynolds numbers up to 12,000. At a particular setting, the belt speed is constant to within $\pm 0.25\%$.

The lower boundary of the cavity is a heat exchanger plate. In addition, the copper belt is in continuous contact with a similar plate. By circulating water of the appropriate temperature through each plate, it is possible to generate a natural convection flow within the cavity. The maximum vertical temperature differential that can be attained is 10 ± 0.05 °C. The four vertical walls of the cavity are adiabatic. This is ensured in practice by adding styrofoam insulation to the side-walls and by maintaining the mean fluid temperature as close to the laboratory ambient temperature as possible.

Finally, the cavity depth (D) can be varied from 150 to 600 mm by lowering the bottom heat exchanger plate. In this study, heat flux measurements were performed at four cavity depths: 150, 300, 450, and 600 mm. These correspond to DAR (DAR = D/B) of 1:1, 2:1, 3:1, and 4:1, respectively. For each case, three temperature differentials were studied: 1, 4, and 8 °C. Furthermore, for each combination of DAR and temperature differential, nine belt-speeds were used providing Re numbers ranging from 0 to 12,000. This resulted in a total of 108 different cases.

Flow visualization technique

Thermochromic liquid crystals possess the ability to change color with temperature, and therefore, can be used to visualize the temperature field in mixed-convection flows. The liquid crystals are encapsulated in microspheres which are advected by the flow, and thereby enable visualization of the flow field as well. For the present study, we chose a chiral nematic type of TLC manufactured by Hallcrest. This particular sample is available in the microencapsulated form with 50–100 μm sized capsules. The active range for this TLC starts at 23 °C and has a bandwidth of 2 °C. A concentration of 0.2 g/l is adequate to visualize the flow satisfactorily.

Specific planes of the cavity were illuminated, as shown in Figure 3. The "end view" refers to the view of the symmetry plane through the end wall, while the "side view" offers a view of a plane parallel to the downstream side wall (DSW) through the upstream side wall (USW). The illumination for both views was provided by an 800-W ILC Technology xenon lamp in conjunction with a slit-and-lens arrangement, which focused the light into a thin (3-mm) sheet. Kodacolor 400 ASA film and an exposure time of 3 seconds with an f stop of 5.6, produced the best results.

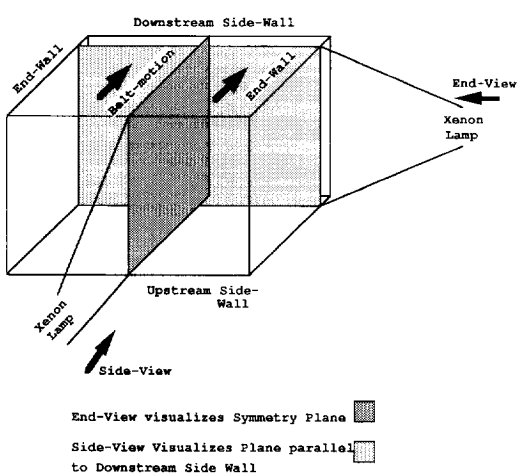

Figure 3 Illuminated planes for flow visualization

Visualization photographs (color) were obtained for $\Delta T = 8$°C, at Re of 3200 and 7500, for all four DARs. In this paper, however, we have included only two representative prints for DAR of 2:1.

Heat flux measurements technique

The heat flux meters used for the present study were microfoil heat flow sensors manufactured by the RdF Corporation. These heat flux meters are in the form of a thin, rectangular strip or foil and are mounted flush on the surface at which the heat flux is to be measured. A good thermal contact between the sensor and the surface can be achieved with double-sided adhesive tape. The heat flux meters used in this study measured 12×30 mm, with a foil thickness of 0.11 mm.

The foil consists of an electrical insulator, in which a number (typically 20) of copper–constantan thermocouple junctions are embedded. The junctions are connected in a single series circuit and are arranged so that alternate junctions are on opposite surfaces of the foil. Therefore, the voltage generated at the leads of the heat flux meter is directly proportional to the difference in the temperatures of the two surfaces, which in turn, depends on the heat flux through the foil. The manufacturer-supplied thermal resistance of the sensors used in our experiments was 5.3×10^{-4} K/(W/m^2) with a response time of 50 Hz.

In our measurement configuration, the heat flux meters were submerged in water for prolonged periods of time. Consequently, the manufacturer-supplied calibration constants could not be relied upon for high accuracy. Therefore, we devised an *in-situ* calibration technique, and recalibration was performed at frequent intervals. On the basis of slight drift in the calibration constants, we estimate that the uncertainty in the heat flux measurements is limited to $\pm 5\%$.

A total of eight heat flux meters were attached to the lower boundary of the cavity, as shown in Figure 4. This particular arrangement was chosen to distribute the measurement locations uniformly over the lower boundary of the cavity, and thus to obtain an accurate estimate of the average, overall heat transfer from the lower boundary. The voltage output of the meters (which typically, is about 6 μvolts for every 100 W/m^2 of heat flux) was then amplified by a factor of 40,000 using an 8-channel amplifier, before digitization. An HP2100 data acquisition system was used to sample the heat flux output at a rate of 100 Hz, for a period of 11.92 minutes. The heat flux for each meter was then analyzed on an HP1000 system, providing time traces and spectra, and the mean heat flux over the entire lower surface was determined by taking the average of all eight heat flux meters. (However, as mentioned previously, this paper focuses specifically on the averaged heat flux values.)

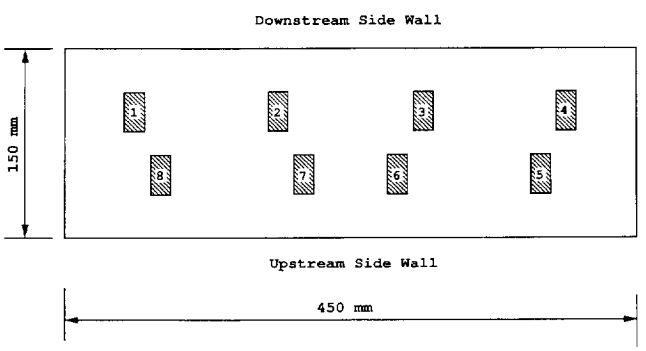

Figure 4 Location of heat flux meters over the cavity floor

Observations

Flow visualization results

Visualization of two perpendicular planes of the cavity provided valuable insight into the nature of the 3-D flow structures in the lid-driven cavity flow. At the outset, the heat exchangers were set to produce the required temperature differential and allowed to run for a period of 24 hours. The two light sources and cameras were then positioned as shown in Figure 3. Next, the belt was started and set at the desired speed, and the flow eventually reached a fully developed state. Subsequently, a measured quantity of TLCs was introduced slowly through a small port in the DSW and distributed uniformly by the mixed-convection flow.

Figures 5a and 5b form an end-view/side-view pair for a DAR of 2:1, ΔT of 8 °C, and Re of 3200. Figure 5a is an end-view picture of the symmetry plane. The belt moves from left to right at the top of the picture. The fluid adjacent to the belt is cold, as it is cooled by the upper heat exchanger plate. This cold fluid (which is red in color) is stripped off at the corner formed by the lid and the DSW and plunges down along the DSW in the form of a wall jet. The inertia imparted to this fluid by the lid is aided by its larger density (the red fluid is colder, and therefore, denser), and the wall jet continues all the way to the floor of the cavity. At the floor, the fluid absorbs heat provided by the lower heat exchanger plate, and the fluid becomes warmer and changes in color to a dark blue (the hot end of the color spectrum). Finally, the warmed-up fluid ascends the USW in the form of a buoyant plume and penetrates into the core of the recirculating fluid.

Figure 5b is the corresponding side-view picture that was exposed 4 seconds after Figure 5a, in a plane parallel to the DSW, and 22 mm from it. It is possible to pick out counter-rotating pairs of longitudinal vortices along the floor, separated at regular intervals in the spanwise direction. These are the Taylor–Görtler-like (TGL) vortices that originate over the concave separation surface of the downstream secondary eddy (DSE) (see Figure 1). The mechanism that generates these vortices involves the centrifugal instability resulting from the flow over a concave surface and have been extensively described in Koseff and Street (1984) and Prasad et al. (1988) for isothermal flows at a DAR of 1:1. Rhee et al. (1985) discovered that TGL vortices also form at a DAR of 1:1 in a mixed-convection flow ($\Delta T = 4$ °C, Re = 3200); however, the size of the TGL vortices are diminished when compared with that of the isothermal case.

Heat flux results

Heat flux measurements were performed in the following manner. The calibrated heat flux meters were attached on the cavity floor at the locations indicated in Figure 4, and the lower plate was moved to the appropriate depth. As in the case of flow visualization, the heat exchangers were run for a period of 24 hours at the required temperatures before data acquisition commenced. The first case studied during an experiment was the natural convection case (lid is stationary Re = 0). Subsequently, the belt was started and the belt speed was set to produce the next Re. Data were acquired only after allowing sufficient time for the new flow conditions to reach a fully developed state

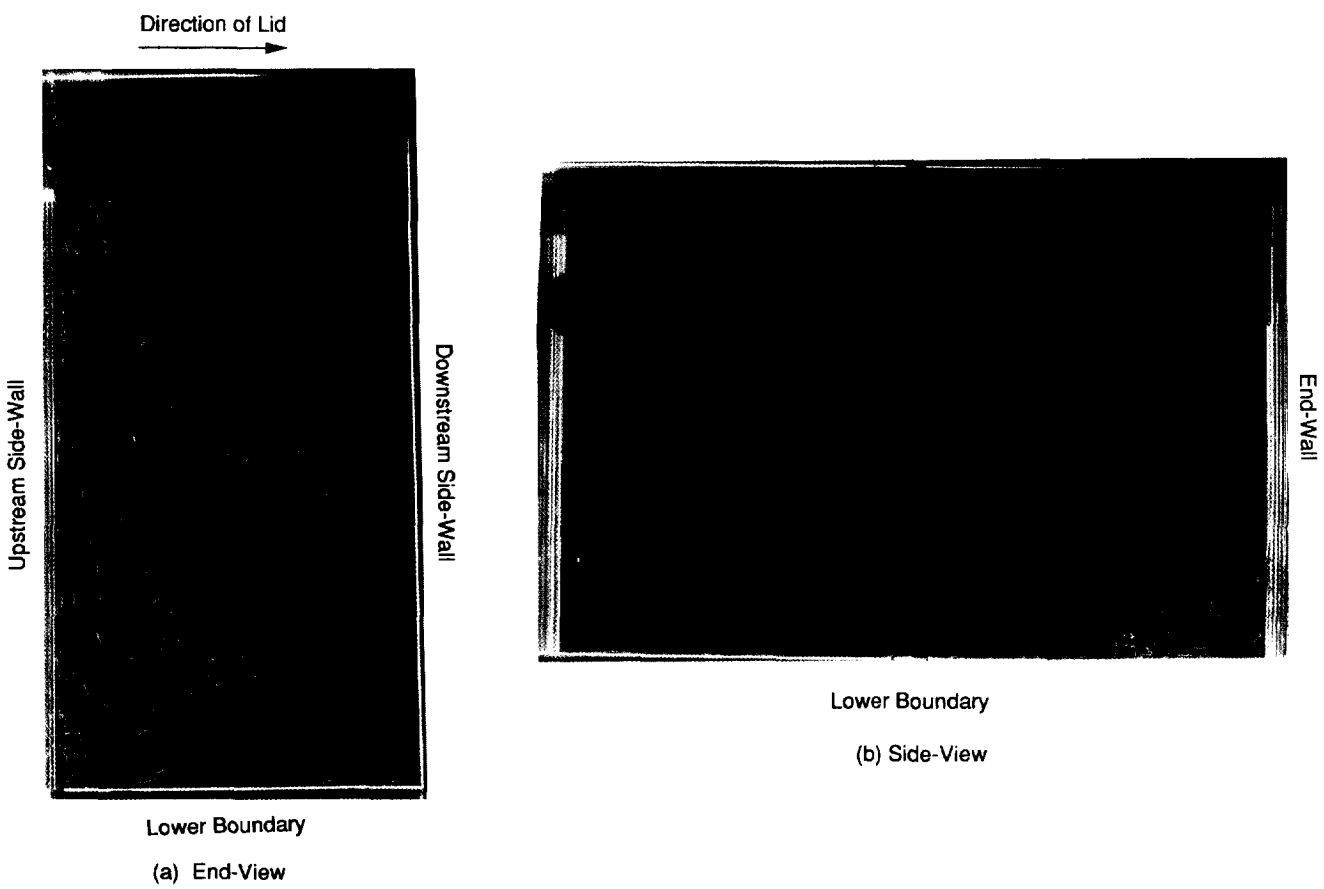

Figure 5 Flow visualization with liquid crystals: DAR 2:1, Re=3200, ΔT=8 °C; (a) symmetry plane (end view); (b) plane parallel to DSW and 20-mm from it (side view)

(about 1 hour). This process was repeated every hour, until the highest Reynolds number had been studied.

Figures 6a, b, c, and d show the mean heat flux over the cavity floor (averaged over all eight heat flux meters for a period of 12 minutes) for DARs 1:1, 2:1, 3:1, and 4:1, respectively. Each plot contains heat flux data for the three temperature differentials, as a function of the Reynolds number. The corresponding uncertainties ($\pm 5\%$) are also indicated. These plots show that the heat flux is strongly influenced by the temperature differential, and at a given ΔT, it usually increases with the Reynolds number. This behavior is seen for all DARs. We see that the DAR seems to have a rather weak influence on the heat flux. However, for the DARs of 3:1 and 4:1, we see that at higher Reynolds numbers (> 8000), the heat flux begins to level off: an increase in Re does not cause an increase in the heat flux. In fact, for the $\Delta T = 1$ °C case at these DARs, the heat flux actually decreases with Re, for $Re > 5000$.

Discussion

The experiments described above were made in a flow driven jointly by shear and buoyancy. The strength of shear-driven motion is given by the Reynolds number Re, and the strength of buoyancy is given by the Grashof numbers Gr. In these experiments, $0 \leq Re \leq 12{,}000$ and $10^7 \leq Gr \leq 5 \times 10^9$. The corresponding range of Gr/Re^2 spanned about four orders of magnitude, from 0.1 to 1000.

The ratio Gr/Re^2 is used traditionally to indicate the relative strengths of the two modes of convection in a mixed-convection environment. Gebhart (1971) deduced from a simple manipulation of the Navier–Stokes equations that the buoyancy effects become noticeable when Gr/Re^2 approaches unity. For $Gr/Re^2 \ll 1$, the forced-convection component controls the heat transfer processes, while for $Gr/Re^2 \gg 1$, buoyancy effects predominate. Based on this principle, Siebers (1983) defined the mixed convection limits for heat transfer from a vertical heated plate in a horizontal stream as $0.7 \leq Gr/Re^2 \leq 10$.

Unfortunately, the ratio Gr/Re^2 cannot be applied universally to every flow configuration. Researchers have often modified this parameter in order to interpret their data. For instance, Wang et al. (1983) delineated the forced-, mixed-, and free-convection regions with the parameters $Gr/Re^{3/2}$. They determined the mixed-convection regime to apply for $10 \leq Gr/Re^{3/2} \leq 400$. Similarly, Imura et al. (1978) found that transition from laminar forced convection to turbulent convection occurred in the range of $100 \leq Gr/Re^{3/2} \leq 300$. Chen et al. (1977) report that for $Gr/Re^{5/2} > 0.05$, buoyancy effects became significant.

One of our objectives was to determine if the ratio Gr/Re^2 could be used to classify the cavity flow driven jointly by shear and buoyancy adequately.

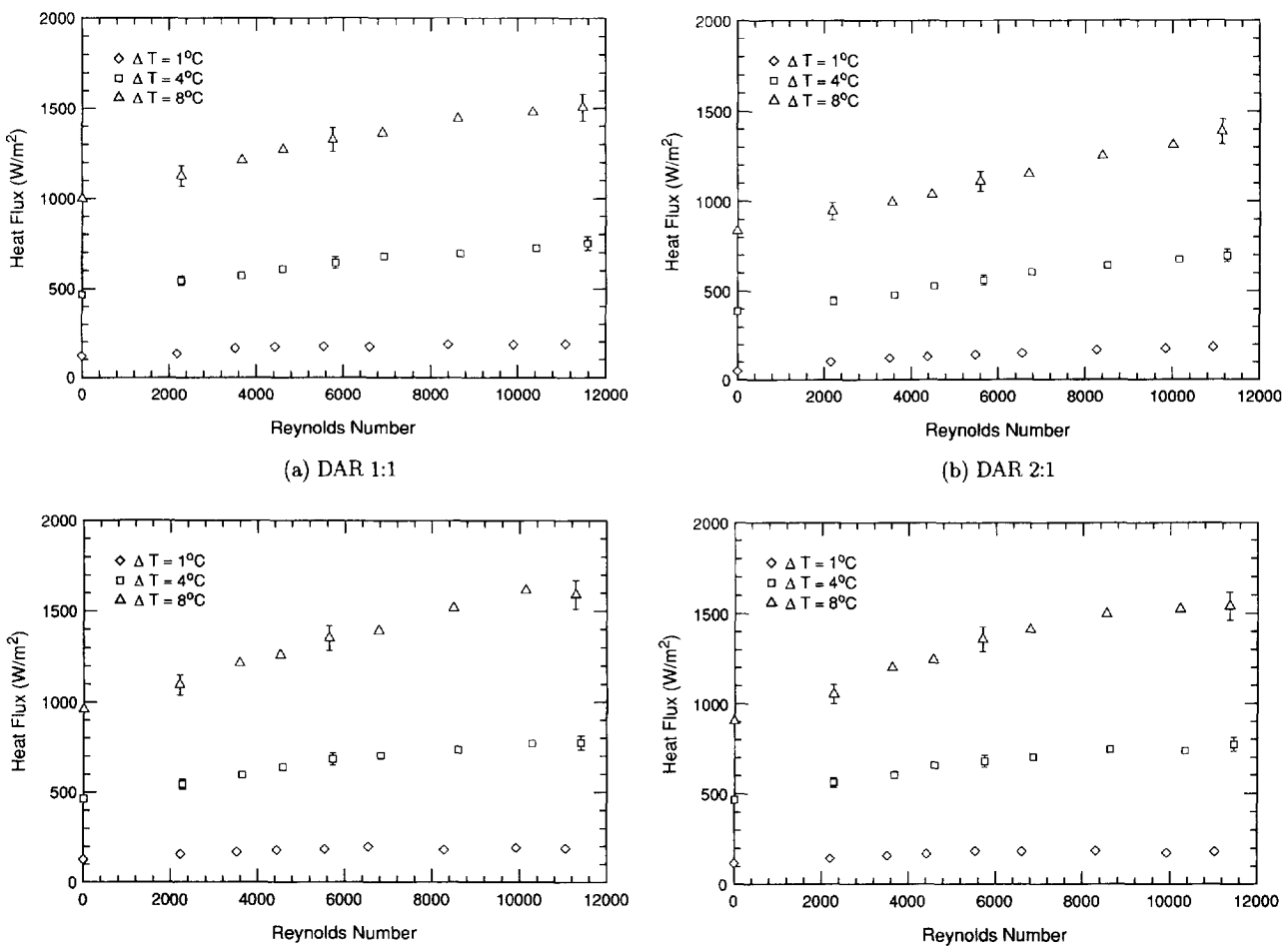

(a) DAR 1:1

(b) DAR 2:1

(c) DAR 3:1

(d) DAR 4:1

Figure 6 Variation of heat flux with Reynolds number and the temperature differential

Free-convection measurements at Re=0

First, we focus on our free-convection heat transfer measurements made at Re = 0. This pertains to the case of Rayleigh–Bénard convection at high Rayleigh number, a problem that has been actively studied over the past few decades. Previous experimental work has shown that the heat flux through the fluid layer may be expressed as

$$\mathrm{Nu} = c_1 \mathrm{Ra}^{1/3} \tag{1}$$

where Nu is the Nusselt number:

$$\mathrm{Nu} = \frac{q}{\Delta T}\frac{D}{k} \tag{2}$$

and Ra is the Rayleigh number:

$$\mathrm{Ra} = \frac{g\beta\Delta T D^3}{\nu\alpha}$$

The 1/3 dependence of Nu on Ra arises from the classical argument that when the convecting layer is highly turbulent, the heat flux q becomes independent of the layer depth D. The implication is that, there exists a thin conduction boundary layer which controls the heat flux adjacent to the lower and upper boundaries; whereas, the rest of the fluid layer is well mixed by turbulence. The thickness of the boundary layer does not change appreciably, even when the total depth D is varied. Consequently, q does not vary with D. Our results for Re = 0 can be fitted by Equation 1 with $c_1 = 0.05$, which agrees reasonably with Goldstein and Tokuda (1980) who give $c_1 = 0.0556$ for convection in water at $10^9 < \mathrm{Ra} < 2 \times 10^{11}$.

The heat transfer coefficient

From Figure 6, the independence of q on D continues, even when Re > 0. This implies that the addition of shear to the buoyancy-driven flow does not alter the heat transfer mechanism adjacent to the boundaries. However, as Re is increased, there is a definite increase in the heat flux for a given ΔT.

The dependence of the heat flux on the temperature differential can be removed by dividing the heat flux by ΔT. This yields the heat transfer coefficient h:

$$h = \frac{q}{\Delta T}$$

Figure 7 shows the variation of the heat transfer coefficient as a function of Reynolds number. This plot contains the data for the three ΔTs and the four DARs. The good collapse of the data points suggests that the heat transfer processes occurring along the cavity floor are fairly uniform for all the cases studied. A least-squares fit of the data provided the following correlation:

$$h = 23.6\,\mathrm{Re}^{0.22} \tag{3}$$

which is also indicated in Figure 7. In this correlation, the units of h are W/m^2 °C. The uncertainty in the calculated value of the heat coefficient is somewhat larger than that in the corresponding heat flux. This additional uncertainty arises because of the error in the measurement in the ΔT (± 0.05 °C), and we expect the relative error to be larger for a smaller ΔT. Therefore, the uncertainty in the heat transfer coefficient is approximately $\pm 10\%$ for the 1 °C case, $\pm 7\%$ for the 4 °C, and $\pm 6\%$ for the 8 °C case. These uncertainties are indicated in Figure 7.

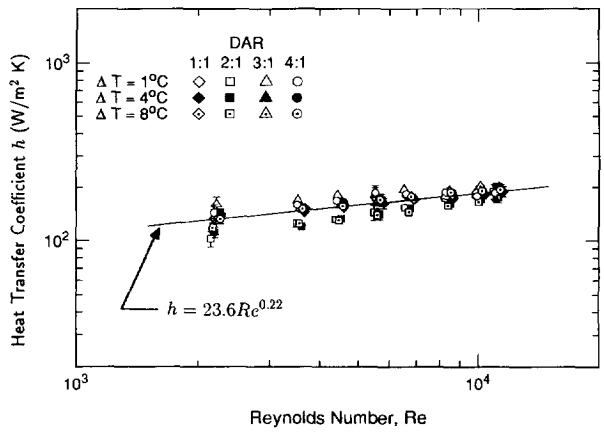

Figure 7 Variation of the heat transfer coefficient with Reynolds number and temperature differential for all DARs

Influence of $\mathrm{Gr/Re^2}$ on Nu

The heat flux data can also be presented in the form of the Nusselt number (Equation 2). The resulting Nusselt numbers for all four DARs were plotted on a single graph, against the ratio $\mathrm{Gr/Re^2}$ (Figure 8). The purpose of plotting Nu against $\mathrm{Gr/Re^2}$ was to identify forced-, free-, or mixed-convection regimes in the $\mathrm{Gr/Re^2}$ spectrum spanning four orders of magnitude from 0.1 to 1000. From Figure 8, the Nusselt number distribution indicates a large spread. However, for a given DAR (especially DAR = 1:1) the data appear to collapse quite well. Therefore, we decided to incorporate the DAR as an extra variable and calculated the coefficients for the following correlation, which is valid for the data from all four DARs.

$$\mathrm{Nu} = 7.96\,\mathrm{Re}^{0.18}\left[\frac{\mathrm{Gr}}{\mathrm{Re}^2}\right]^{-0.02}\left[\frac{D}{B}\right]^{1.1} \tag{4}$$

The corresponding least-squares fit is shown in Figure 9. The surprising aspect of this correlation is that the exponent in $\mathrm{Gr/Re^2}$ is close to zero (in fact, owing to experimental errors in the measurement of heat flux and temperature, the exponent may be safely rounded off to zero; however, we have deliberately retained the $\mathrm{Gr/Re^2}$ term in the correlation in Figure 9 to highlight this unexpected result). The result is unexpected given

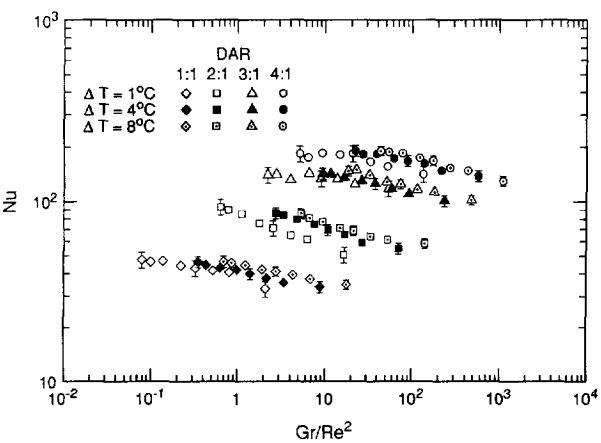

Figure 8 Variation of the Nusselt number with $\mathrm{Gr/Re^2}$ for all DARs

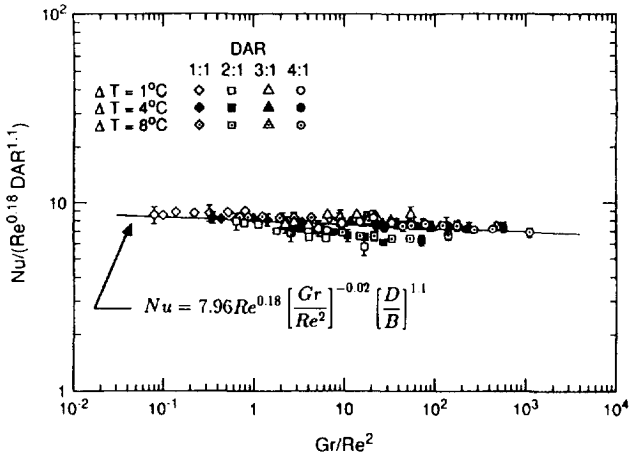

Figure 9 Variation of the Nusselt number as a function of Reynolds number, DAR, and Gr/Re^2

the large range of variation of Gr/Re^2 from 0.1 to 1000, and the traditional belief that $Gr/Re^2 \sim 1$ separates the natural convection regime from the forced-convection regime.

Second, the coefficient for DAR is close to unity, which indicates that the Nusselt number increases almost linearly with DAR (i.e., q is independent of D). In other words, we see that the addition of shear to the buoyancy-driven flow does not alter the fact that the heat transfer is governed by effects that are restricted to a small thickness adjacent to each boundary. The rest of the fluid layer is highly turbulent, disorganized, and well-mixed (Figure 5) very similar to the free-convection situation. Figure 5(a) shows that for $Re > 0$, the flow along the walls of the cavity is well organized and dominated by inertia. For instance, the region adjacent to the DSW is always occupied by a cold, plunging wall jet, while the fluid adjacent to the USW is a warm, buoyant plume. In addition, the lid and the floor have boundary-layer flows attached to them. In contrast, the internal, core region of the recirculating fluid is dominated by the more chaotic, natural convection flow structures.

The pattern of a well-organized boundary-layer flow with a chaotic internal flow, seen in Figure 5(a) for DAR = 2:1, is exactly duplicated at DARs of 1:1, 3:1, and 4:1. Therefore, because the flow dynamics over the cavity floor are similar for all DARs, we expect the magnitudes of the heat transfer coefficient to exhibit a similar behavior over a wide range of DARs and ΔTs.

Third, the coefficient of Re in Equation 4 of 0.18, reflecting a rise in heat transfer rates at the upper and lower boundaries as the lid speed is increased. This result corroborates the correlation presented in Equation 3. $Re^{0.18}$ is a fairly weak dependence when compared to $Re^{1/2}$ seen, for example, in the Pohlhausen relationship for laminar flow over an isothermal flat plate. However, despite the apparent similarities between the flow over the lower boundary of the lid-driven cavity and Blasius-type flow over a flat plate, there exist significant differences. For instance, as seen in Figure 5(a), the flow over the lower boundary may be divided into three zones: (1) impingement of the wall jet as it descends along the DSW with the lower boundary; (2) attached flow over the lower boundary; and (3) separation or updraft region near the USW. Moreover, the effect of buoyancy (cold plumes dropping off the upper boundary layer and hot plumes rising from the lower boundary layer) destabilizes the boundary-layer flow. Consequently, it is improbable that the $Re^{1/2}$ behavior would be replicated by the lid-driven cavity flow.

From Equation 4 we see that Nu increases with Re, indicating that shear does influence heat transfer. However, we also see that Nu varies almost linearly with D (i.e., it varies as $Gr^{1/3}$) indicating the influence of natural convection. It is appropriate to say that forced and natural convection effects actually complement each other: The shear imparted by the lid drags cold fluid towards the DSW. The shear-driven, descending wall jet is aided in its downward motion along the DSW because of its colder (denser) nature. At the lower boundary, the boundary-layer flow is heated up and is driven upwards not only by the remnants of shear but also by the additional buoyancy generated along the lower boundary. Hence, in this configuration and for the range studied, the flow shows the combined effects of forced and free convection. Both effects operate seamlessly, as confirmed by the complete lack of sensitivity to Gr/Re^2 over the entire range.

The Stanton number

From the discussion in the preceding paragraph, it is apparent that the heat flux q is independent of cavity depth D, weakly dependent on Re, and independent of Gr/Re^2. In fact, Equations 3 and 4 show very clear similarities. If we neglect the term involving Gr/Re^2 (on account of its very small exponent) and approximate the exponent of D/B as unity, then Equation 4 can be rewritten in a form very similar to Equation 3 ($h \approx C\mathrm{Re}^{0.18}$), where C is a constant ($C = 8k$ W/m^{2}K). This exercise reveals that the heat transfer coefficient h adequately represents the heat transfer within the lid-driven cavity.

However, Equation 3 relates a dimensional quantity h to a nondimensional number Re. This drawback can be circumvented by employing the Stanton number:

$$\mathrm{St} = \frac{h}{\rho c_p U_B}$$

Figure 10 displays the Stanton number variation with Re for all the DARs and ΔTs studied in this investigation. The least squares fit shown in Figure 10 is given by:

$$\mathrm{St} = 0.94\,\mathrm{Re}^{-0.78}$$

The uncertainty in St is essentially equal to the uncertainty in the corresponding h on account of the low error in U_B; this uncertainty is also indicated in Figure 10.

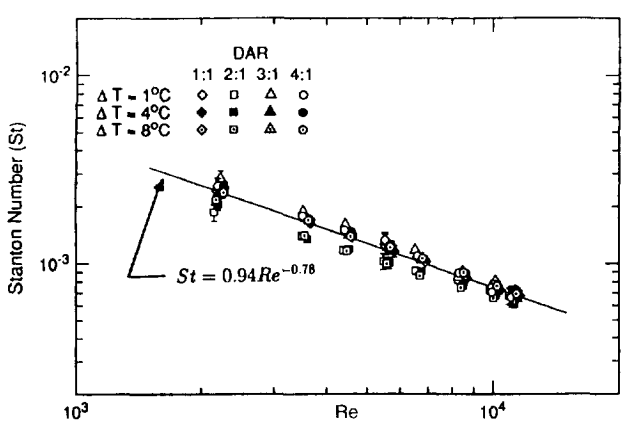

Figure 10 Variation for the Stanton number with Reynolds number and temperature differential for all DARs

Conclusions

Flow visualization and heat flux measurements have been conducted in a bottom-heated, lid-driven cavity flow. The range of Reynolds numbers studied were from 0 to 12,000. The vertical temperature differential, as well as the cavity depth, were varied to produce Grashof numbers from 10^7 to 5×10^9. The corresponding Gr/Re^2 varied between 0.1 to 1000.

Our results indicate the following.

(1) The heat transfer coefficient (obtained by dividing the averaged heat flux over the entire floor by the temperature differential) is insensitive to Gr/Re^2 for the range mentioned above. Flow visualization studies (for DARs 1:1, 2:1, 3:1, and 4:1) indicate that this is because the nature of the flow adjacent to the cavity floor remains unchanged with DAR and ΔT.

(2) The heat transfer within the cavity is independent of Gr/Re^2 over the range studied. However, the fact that q is independent of D merely indicates that $Nu \sim Gr^{1/3}$. This relationship is expected for pure free convection; our results indicate that the relationship holds even when external shear is imparted to the flow. The inference is that both free- and forced-convection effects are important and operate seamlessly over the Gr/Re^2 range studied.

(3) The low exponent on the Reynolds number $Re^{0.18}$ when compared with the Blasius flow exponent of $Re^{1/2}$, confirms the flow visualization results that the flows along the upper and lower boundaries of the cavity are significantly different from Blasius-type flow over a flat plate. Also, buoyancy destabilizes the boundary layer, adding to the deviation from the Blasius $Re^{1/2}$ behavior.

Acknowledgments

This work was supported by the Department of Energy under Grant DE-FG03-84ER13240. The authors appreciate the valuable contributions of R. L. Street, and R. J. Moffat in interpreting the experimental results.

References

Cha, C. K. and Jalurai, Y. 1984. Recirculating mixed convection flow for energy extraction. *Int. J. Heat Mass Transfer*, **27**, 1801–1812

Chen, T. S., Sparrow, E. M. and Mocoglu, A. 1977. Mixed convection in a boundary layer flow on a horizontal plate. *J. Heat Transfer*, **99**, 66–71

Gebhart, B. 1971. *Heat Transfer*, 2nd ed. McGraw-Hill, New York, 388–397

Goldstein, R. J. and Tokuda, S. 1980. Heat transfer by thermal convection at high Rayleigh numbers. *Int. J. Heat Mass Transfer*, **23**, 738–740

Imura, H., Gilpin, R. R. and Cheng, K. C. 1978. An experimental investigation of heat transfer and buoyancy-induced transition from laminar forced convection to turbulent free convection over a horizontal isothermally heated plate. *J. Heat Transfer*, **100**, 429–434

Kays, W. M. and Crawford, M. E. 1993. *Convective Heat and Mass Transfer*, 3rd ed. McGraw-Hill, New York, 413–414

Koseff, J. R. and Street, R. L. 1984. The lid-driven cavity flow: A synthesis of qualitative and quantitative observations. *J. Fluids Eng.*, **106**, 390–398

Lloyd, J. R. and Sparrow, E. M. 1970. Combined forced and free convection flow on vertical surfaces. *Int. J. Heat Mass Transfer*, **13**, 434–438

Muñoz, D. and Zangrando, F. 1986. Mixing in a double-diffusive, partially stratified fluid. SERI/TR-252-2942, Solar Energy Research Institute, Golden, Colorado, USA

Prasad, A. K., Perng, C-Y and Koseff, J. R. 1988. Some observations on the influence of longitudinal vortices in a lid-driven cavity flows. In *A Collection of Technical Papers*, Part 1, AIA/ASME/SIAM/APS 1st National Fluid Dynamics Congress, Cincinnati, OH, 288–295

Rhee, H. S., Koseff, J. R. and Street, R. L. 1985. Visualization of natural and mixed convection flows in a cavity, *Proc. Int. Symposium on Refined Flow Modeling on Turbulence Measurements*, University of Iowa, Iowa City, IA, I11, 1–9

Siebers, D. L. 1983. Experimental mixed convection heat transfer from a large vertical surface in a horizontal flow. Ph.D. thesis, Stanford University, Stanford, CA, USA

Wang, G. S., Incropera, F. P. and Viskanta, R. 1983. Mixed-convection heat transfer in a horizontal open-channel flow with uniform bottom heat flux. *J. Heat Transfer*, **105**, 817–822